EARTH SURFACE PROCESSES AND LANDFORMS
Earth Surf. Process. Landforms **45**, 2118–2133 (2020)

Published online 8 May 2020 in Wiley Online Library
(wileyonlinelibrary.com) DOI: 10.1002/esp.4870

Significance of boulder shape, shoreline configuration and pre-transport setting for the transport of boulders by tsunamis

Jan Oetjen,[1]* Max Engel,[2] Shiva P. Pudasaini[3] and Holger Schuettrumpf[1]
[1] Institute of Hydraulic Engineering and Water Resources Management, RWTH Aachen University, Aachen, Germany
[2] Institute of Geography, Heidelberg University, Heidelberg, Germany
[3] Geophysics Section, Institute of Geosciences, University of Bonn, Bonn, Germany

Received 19 November 2019; Revised 20 March 2020; Accepted 26 March 2020

*Correspondence to: Jan Oetjen, Institute of Hydraulic Engineering and Water Resources Management, RWTH Aachen University, 52056 Aachen, Germany.
E-mail: oetjen@iww.rwth-aachen.de

ESPL
Earth Surface Processes and Landforms

ABSTRACT: Research on tsunami-induced coarse-clast transport is a field of rising interest since such deposits have been identified as useful proxies for extreme-wave events (tsunamis, storm waves) that provide crucial information for coastal hazard assessment. Physical experiments are, beside *in-situ* observations, the foundation of our understanding of how boulders are transported by tsunamis and provide clues to the development of empirical equations and numerical models describing the processes and fundamental mechanics. Nevertheless, investigating tsunami-induced boulder transport is a comparatively young discipline and only a few experimental studies focusing on this topic have been published so far. To improve the knowledge on nearshore tsunami hydrodynamics, physical experiments utilizing real-world boulder shapes have been carried out simulating three different shore types in a wave flume. Crucial insights were gained into boulder transport hydrodynamics and data resulting from the experiments were analysed in an empirical, statistical, quantitative and qualitative manner. The regular cuboid boulder – one of the specific shapes used in the experiments – showed the longest transport distances compared to a complex, natural boulder and a flat cuboid boulder, but also significant fluctuations regarding the total transport distance. The experiments indicate a strong influence of the shore shape on boulder transport behaviour. Experimental setups of increased mean transport distances also led to a higher spreading of results. This spreading was further amplified between the idealized-shaped cuboid and the complex-shaped boulder, which is associated with a lower drag coefficient. Due to the highly sensitive boulder reaction to divergent experimental setups, the need to recognize boundary conditions overcoming commonly considered parameters (e.g. roughness or Flatness Index) in field studies and numerical models is underlined. Beside the strong influence of initial boulder submergence and alignment, both the boulder shape and shore type influence the boulder transport pattern, increasing the total transport distance by more than 350% in some cases. © 2020 The Authors. Earth Surface Processes and Landforms published by John Wiley & Sons Ltd

KEYWORDS: boulder transport; hydraulic experiment; statistical analysis; boulder shape; flatness index

Introduction

Subaerial coarse-clast deposits along rocky coasts (mostly boulders to fine blocks *sensu* Blair and McPherson, 1999) are valuable indicators for past extreme-wave impacts (storm waves, tsunamis). While earliest reports on their transport by tsunamis date back to the nineteeth century (Neale, 1885), their systematic use to reconstruct major tsunamis or storms started only in recent decades (e.g. Bourrouilh-Le Jan and Talandier, 1985; Nakata and Kawana, 1995; Scheffers and Kelletat, 2003; Etienne et al., 2011; Engel et al., 2016). Nott (1997, 2003) was the first to introduce equations, which describe the initiation of boulder motion and, thus, enable inferences on the physical characteristics of tsunamis and storm waves. This and other comparable approaches have been widely used since then (e.g. Noormets et al., 2004; Pignatelli et al., 2009; Paris et al., 2010; Etienne et al., 2011; Nandasena et al., 2011; Engel and May, 2012; Sugawara et al., 2014; Watanabe et al., 2019), even though it is commonly understood that their simplification of the transport process leads to significant uncertainty (Sugawara et al., 2014; Oetjen et al., 2017; Bressan et al., 2018; Nandasena, 2020). These efforts are today complemented by physical experiments on boulder transport (e.g. Imamura et al., 2008; Bressan et al., 2018) and forward numerical models (e.g. Zainali and Weiss, 2015) in order to improve our understanding of the transport of boulders by extreme waves and to use boulders as a proxy for coastal hazards in a more reliable way. However, the number of studies of boulder transport based on laboratory experiments is surprisingly low and only a limited spectrum of parameters has been systematically investigated (Oetjen

et al., 2020). Imamura et al. (2008) studied cubic boulders with a varying Flatness Index (FI) = $(a + b)/2c$ (a = long boulder axis in cm; b = boulder height in cm; c = boulder width in cm) and density in a 10 m-long flume ending in a uniformly inclined shore (1:10). The cubic bodies of low FI tend to roll or saltate, while the authors also found a significant inverse relationship between FI and transport distance. Nandasena and Tanaka (2013) conducted experiments in a comparable setup with a slope of 1:20, boulders with an FI of 1 to 3, different densities, different pre-transport orientations, and a range of wave heights and velocities. They found that shape and bottom friction significantly influence the transport mode: while flat boulders and low bottom friction support sliding, cube-like boulders and higher bottom friction support rolling. After initiation of transport, the main (resp. long) axis always aligns perpendicular to the flow and, thus, influences the overall transport distance (Nandasena and Tanaka, 2013). Liu et al. (2015) used an 18 m-long flume with a central inclined section (3.75:100) and quantitatively investigated the influence of wave velocity and height as well as the pre-transport setting of the main axis of a cuboid boulder. The authors found sliding to be the dominant transport mode and a generally shorter distance in the case of rolling transport. Furthermore, transport distance was found to be sensitive to bore height and velocity (Liu et al., 2015).

A range of parameters relevant to boulder transport by waves remains unstudied. In this article, we investigate the influence of boulder shape on transport mode and transport distance. We use idealized cuboid boulders, as in previous studies, and compare their performance with subrounded, naturally shaped clasts. Furthermore, we investigate the pre-transport setting and the influence of the coastal setup (bathymetry, topography) on transport mode and transport distance by using three different shore models, a uniformly inclined one, one with altering inclination and a stepped shore.

Methods

Boulder models used in the experiments

The complex, naturally shaped boulder model employed in this study is based on a well-studied cliff-top clast from the island of Bonaire, Leeward Antilles ('largest boulder' in Watt et al., 2010; BOL 2 in Engel and May, 2012) (Figure 1). The boulder has main axes of a = 8.7 m, b = 4.8 m and c = 3.8 m, a density of c. 2.2 g/cm^3, a weight of 170 t (previously estimated to be 150 t) and is located approximately 45 m from the shore at an elevation of c. 6.8 m a.s.l. (above mean sea level). It was sourced from the cliff edge, as the upper part of the intertidal bio-erosive notch is still visible. BOL 2 has an irregular, elongated shape, its main axis is parallel to the shoreline and it is located on a pedestal, indicating that transport occurred hundreds if not thousands of years ago (Engel and May, 2012). Based on its size, setting and hydraulic parameters inferred from initiation-of-motion criteria, as well as a comparison with boulder-transport patterns during recent high-category hurricanes on Bonaire, transport by a tsunami was considered a probable scenario (Watt et al., 2010; Engel and May, 2012).

For measuring the boulder, structure-from-motion (SfM) was applied (cf. Gienko and Terry, 2014; Boesl et al., 2019) by using nearly 400 separate overlapping images of a Sony DSC-HX200V camera (constant focal length of 0.5 cm) and Agisoft Photoscan, Meshlab and Autodesk Fusion360 software. The SfM model was completed by creating artificial plain surfaces where images are either absent, such as at the underside, or where they do not overlap sufficiently, as on the top. The SfM model has a volume of 77 m^3 – compared to 68 m^3 derived from a low-resolution DGNSS (differential global navigation satellite system) point cloud by Engel and May (2012) – resulting in a weight of 170 t. The SfM model was used to print

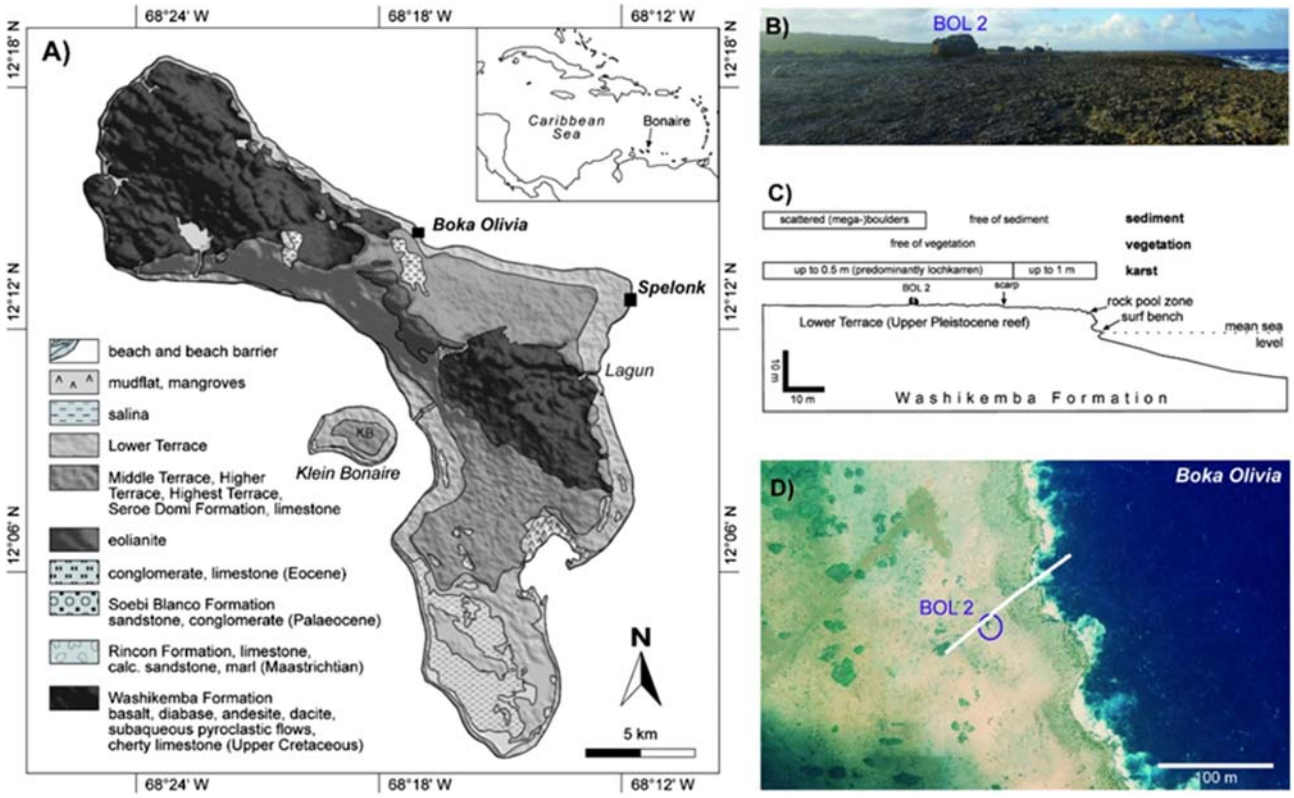

Figure 1. (A) Simplified geological map of the island of Bonaire showing the elevated 'Lower Terrace' unit (B, C) that forms a quasi-stepped cliff coast and (D) represents the location of the complex-shaped boulder BOL 2 (Engel and May, 2012), which was considered in this experimental study. Data sources for the map are given in Engel and May (2012). [Colour figure can be viewed at wileyonlinelibrary.com]

a positive template of polylactide (PLA) in a scale of approximately 1:50. The PLA template was then used to create a negative model of silicone rubber (WACKER ELASTOSIL® M 4642) to cast the final boulder model from grouting mortar.

The final 1:50 complex boulder model BOL 2 has (box of outer boundaries; see Figure 2) main axes of a = 17.5 cm, b = 9.6 cm and c = 7.6 cm (FI = 1.58), a volume of 700 cm^3 and a weight of 1485 g. Two cuboid boulder models with similar volume and weight were created (Figure 2):

- Regular cuboid boulder (approximately 1480 g): a = 14 cm, b = 8 cm, c = 6 cm (FI = 1.83); this shape is quite common in carbonate reef-top settings.
- Flat cuboid boulder (approximately 1430 g): a = 13.7 cm, b = 15.5 cm, c = 3 cm (FI = 4.9); this shape is particularly common in beachrock and sandstone-type environments.

All boulder models were created from the same material with a density of approximately 2.2 g/cm^3. Density deviations in a neglectable amount occur due to inhomogeneities during the casting.

Experimental setup

The boulder-transport experiments were conducted in the large tilting flume of the Institute of Hydraulic Engineering and Water Resources Management (IWW) of the RWTH University in Aachen (Germany). The flume has a usable length of 25.5 m and a width of 1 m. The tsunami is modelled as a broken bore using a combination of specific pumping time, valve position and a low barrier that initiates wave breaking (Figure 3). The pumping time and the valve position are remotely adjusted for the creation of bores of different heights, lengths and velocities with a high reproducibility (Supporting Information Figure S1). Two pumps (400 l/s conveying capacity each) extract the water from an underground reservoir through a perforated metal plate and multiple pipes for homogenization/abating of the flow. Three meters after the homogenization, the flow passes a small barrier, which initiates the wave. In front of the barrier, the water level is at between 0.13 m (standard) and 0.2 m above ground. The wet bed has an extent of approximately 16 m ending at the shore model, for which we use three different types:

- Type 1: a uniformly inclined slope (approximataly 7.5°; Figure 4a), a scenario that is used in all existing experimental studies on boulder transport by tsunamis (Imamura et al., 2008; Nandasena and Tanaka, 2013; Liu et al., 2015)
- Type 2: a compound slope with two different angles (11° and 4°; Figure 4b)
- Type 3: three stepped, horizontal platforms (Figure 4c) that are based on the natural setting of elevated cliff coastlines and abrasive shore platforms. The first two steps are 0.1 m in height, while the final step is 0.2 m high. The discrepancy in height is due to the aim of keeping the final height the same as for shore Types 1 and 2 by preserving the possibility for a vertical shift of the boulder.

All shore types end on a plateau of 1 m length made from polyvinyl chloride (PVC). The experimental programme encompasses multiple setups regarding the submergence (submerged, partially-submerged, subaerial) and alignment (0°, 45°, 90°) of the main boulder axis for each shore model (Figure 4, Table 1). The submergence factor is kept constant over the experiments related to the water column above the boulder (submerged case), the height of the boulder protruding from the initial water level (partially-submerged) and the distance between water surface and boulder (subaerial). Diverting from this, for the stepped shore (Type 3) the water level was varied for the submerged case (Figure S10). The actual positions (distance to shore model tip in centimetres) differ depending on boulder model and shore type and are shown in detail in the associated paragraphs.

The wave height was measured by ultrasonic wave gauges at two positions, one directly at the tip of the shore model and one 3 m further away. Flow velocity was recorded by an impeller velocimeter 1.5 m in front of the shore model. The boulder transport was additionally captured by two GoPro cameras in bird's eye view right above the shore model and at the side of the flume, respectively (Figure S2). The friction coefficient was estimated by calculating the necessary force to drag the boulder across the shore and subsequent division of the necessary drag force by the body-specific weight force. This leads to varying friction coefficients μ of 0.21 [–] to 0.6 [–] depending on boulder shape and shore inclination. The friction coefficients for all setups are listed in Table 2.

While the original boulder was scaled in a scale of approximately 1:50, all other parameters were chosen according to the flume dimensions. The exact weight of the original boulder

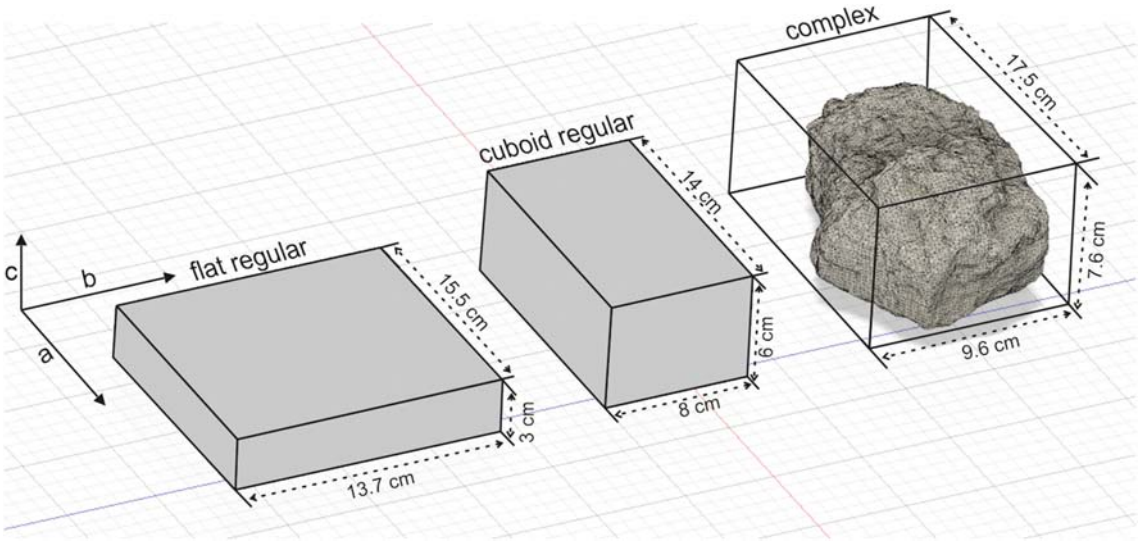

Figure 2. The three applied boulder models. From left to right: regular flat boulder, regular cuboid boulder and complex boulder. [Colour figure can be viewed at wileyonlinelibrary.com]

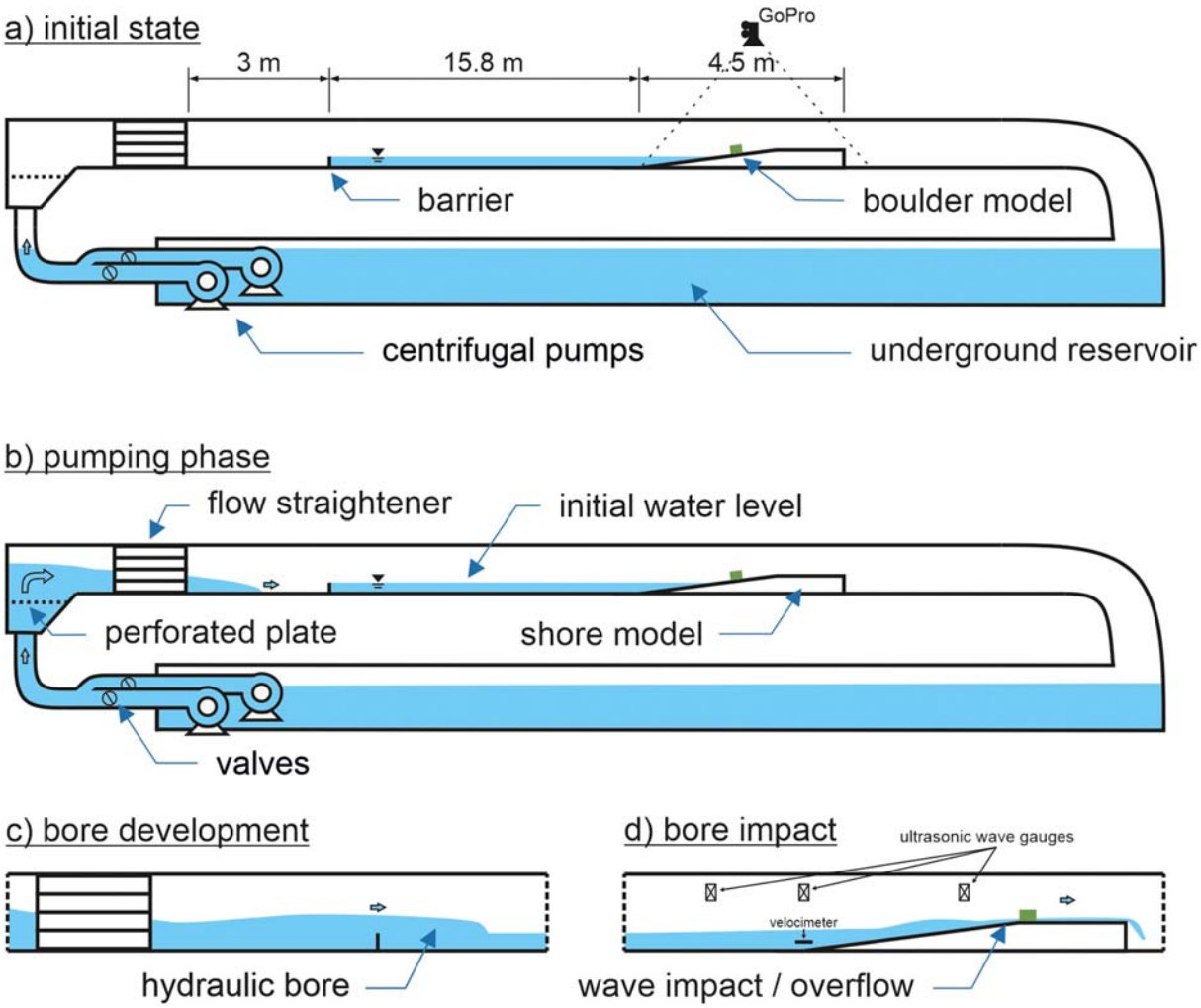

Figure 3. Experimental setup: (a) initial state; b) pumping begins. Water is pumped from the reservoir through a perforated plate and flow straightener on the flat flume bed. (c) Flow passes the straightener and approaches the installed barrier, while the hydraulic bore is generated on the wet bed. (d) The bore approaches the shore model and impacts the boulder. [Colour figure can be viewed at wileyonlinelibrary.com]

BOL 2 is difficult to determine due to the unknown heterogeneous density and density distribution of the boulder, as well as the remaining uncertainties regarding its exact volume. Thus, the boulder replica was made of a material with a density similar to the assumed bulk density of the original BOL 2 (2.2 g/cm^3; Engel and May, 2012). The experiments were conducted using freshwater which consists of a density approximately 3% below the density of seawater. This difference is neglected in the experiments since its influence is overprinted by the other scaling effects (e.g. roughness) and is furthermore constant over all conducted experiments.

Video processing

Boulder celerity and transport distance after the bore impact were analysed using video recordings. All shore models contained a 10 cm × 10 cm grid, which allows for a computer-assisted evaluation of boulder movement. For analysis of the transport, a Matlab® script was established to calculate position changes between video frames using the underlying grid as reference. The reference distance was refreshed at characteristic time intervals of the transport: (1) Due to the inclination of Types 1 and 2 shoreline models and the fish lens of the GoPro camera, the reference distance varied over the entire transport distance and had to be updated periodically. (2) In case of Type 2, the reference was updated when the boulder reached the inclination break. (3) When the flow surrounded or submerged the boulder, the view was disturbed due to the refraction of light. The boulder movement and bore velocity were eventually calculated by recording the position of a characteristic pixel of the boulder or bore tip over two different frames with respect to the passed time-interval, which is, in this case, equivalent to the frames-per-second of the video.

Results

Bore dynamics

The bore hydraulics differed slightly in the three shore setups and were further altered by applying individual pump and valve preferences. Only one wave was applied over all experiments on shore Type 1, since the main task was to gain statistically robust results (see wave profile in Figure S2). Here, the bore reached a height of *c.* 0.16 m right in front of the shore and a velocity of v = 0.73 m/s. From video analysis, the run-up velocity of the bore immediately before the impact on the boulder is 2 m/s with a height of h = 0.055 cm, resulting in a Froude number of Fr = 2.65 [–].

Two different bores with h = 0.17 cm and h = 0.16 cm were generated in the shore Type 2 setup. The bore velocity at wave gauge 3 reached 0.87 m/s and increased to 2.0 m/s (Fr = 4.5) during the run-up. The first wave impact was followed by strong reflections and turbulences in the flume (Figure 5), which resulted from the following pushing wave and which reflect a modified tsunami profile, if compared with an ideal one

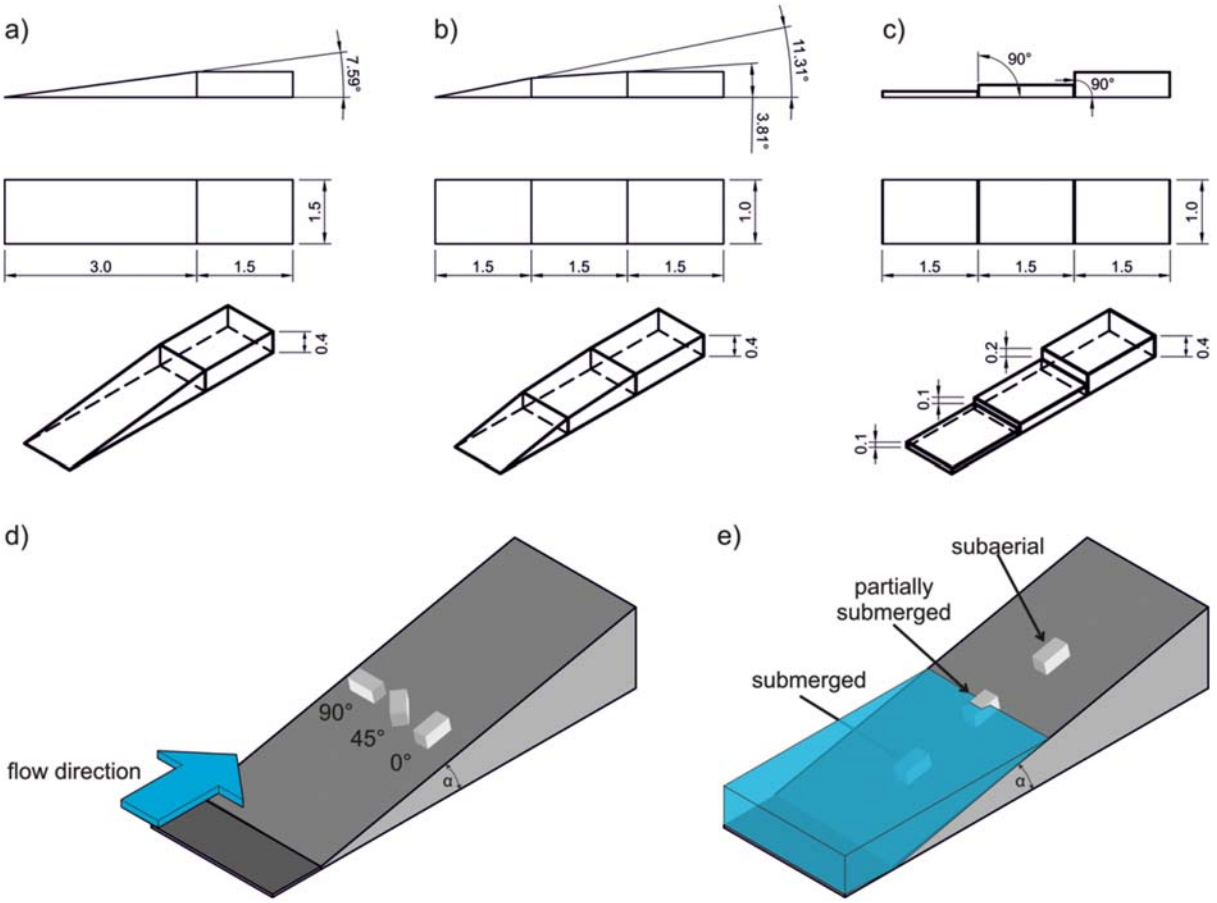

Figure 4. Top: Applied shore types. (a) Type 1 with a uniform inclination; (b) Type 2 with two different inclinations; (c) Type 3, stepped shore resembling the shore of the type site of BOL 2 on Bonaire (Figure 1). Bottom: initial boulder setups. (d) Initial alignment to the flow: 90°, long axis perpendicular to the flow; 45°, long axis at a 45° angle to the flow; 0°, short boulder axis perpendicular to the flow. (e) Pre-transport positions in relation to water level. [Colour figure can be viewed at wileyonlinelibrary.com]

as, e.g. in Pedersen and Gjevik (1983). On shore Type 2, tracking of the boulder using an inertial measurement unit (IMU) was tested. The cavity for the IMU inside the boulder (radius of 1.5 cm, depth 10 cm) results in a slightly lower volume (approximately 5% compared to shore Type 1 and 3) and deviating hydrodynamic boulder behaviour.

In the setup of shore Type 3, the bore approached the shore with a velocity of 0.3 m/s, which increased to 2.2 m/s on the shore at an initial water level of 14 cm. With an initial water level of 0.20 m, the bore approached the shore by approximately 1.93 m/s before the first boulder impact.

Table 1. Overview of the experimental setup.

										Total setups
Shore Type 1										
Boulder shape	Complex			Regular cuboid			Flat cuboid			
Alignment	0°			0°			0°			9
Submergence	s	p-s	sa	s	p-s	sa	s	p-s	sa	
Shore Type 2										
Boulder shape	Complex			Regular cuboid			Flat cuboid			
Alignment	0°	45°	90°	0°	45°	90°				18
Submergence	s	s	s	s	s	s				
	p-s	p-s	p-s	p-s	p-s	p-s				
	sa	sa	sa	sa	sa	sa				
Shore Type 3										
Boulder shape	Complex			Regular cuboid			Flat cuboid			
Alignment	0°	45°	90°	0°	45°	90°				18
Submergence	s	s	s	s	s	s				
	p-s	p-s	p-s	p-s	p-s	p-s				
	sa	sa	sa	sa	sa	sa				

Boulder shape depicts the type of applied boulder (complex, regular cuboid, flat cuboid). Alignment describes the initial boulder alignment to the flow: 0°, long axis perpendicular to the flow; 90°, short axis perpendicular to the flow. Submergence indicates the initial boulder setting (s = submerged: boulder completely under water; p-s = partially submerged: part of the boulder is beneath the water surface; sa = subaerial: the boulder is completely above the water surface)

Boulder transport

Experimental designs and numbers of runs (238 runs overall) for the uniformly inclined shore model (Type 1) are summarized in Supporting Information Table S1. Ninety-nine runs were conducted with the complex boulder, 85 runs with the regular cuboid boulder and 54 runs with the flat cuboid boulder. The experimental runs on the shore Type 2 setup (non-uniformly inclined) encompass 149 runs, while on the stepped shore (Type 3) 230 runs were conducted.

Table 2. Calculated coefficients of friction (μ [-]) for wet conditions depending on shore inclination (3.8°, 7.6°, 11.3°) and boulder type (flat cuboid, complex, regular cuboid)

Bed	*Flat cuboid*	*Complex*	*Regular cuboid*
0° (horizontal)	0.29	0.21	0.21
3.8°	0.4	0.34	0.38
7.6°	0.45	0.42	0.45
11.3°	0.6	0.54	0.45

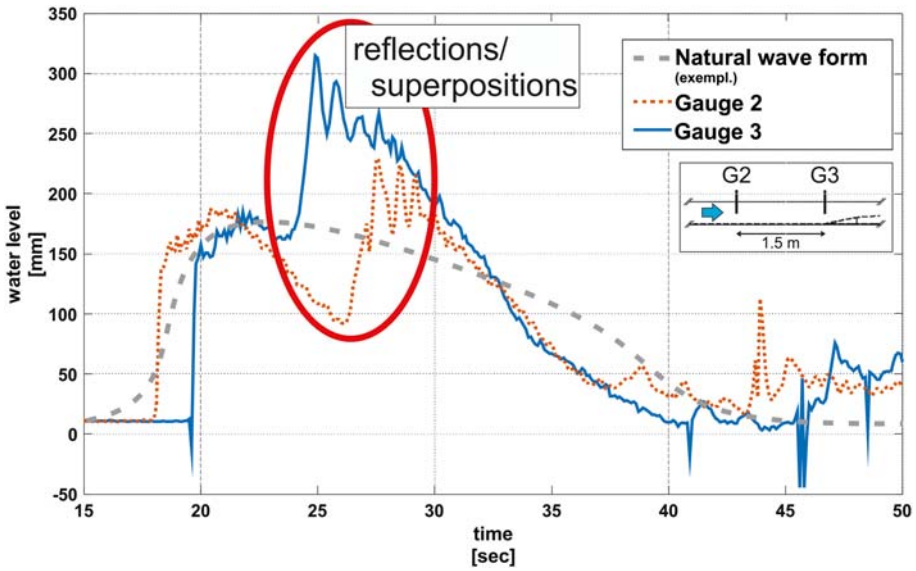

Figure 5. Wave profile 1.5 m in front of the shore and at shore tip on shore Type 2 and 17.2 cm bore height. Idealized tsunami profile (natural wave form) after Pedersen and Gjevik (1983). [Colour figure can be viewed at wileyonlinelibrary.com]

Type 1 – uniformly inclined shore model

In the subaerial pre-transport setting, the boulders were placed on the slope 18 cm from the water surface and centred in *y* direction (channel width). For the partially submerged case, the boulders were placed in a way that half of the object was immersed (Figure S3). The main axis of the boulders was aligned perpendicular to the flow.

Boulder transport occurred in two or three steps, respectively. After the first wave impact, a short time lag occurred before boulders were transported (Table 3) at low velocities for a few centimetres (Figure 6). While the complex and the flat cuboid boulders then stopped for < 0.5 s, the regular cuboid boulder only slowed down before again experiencing acceleration by the second wave (Figure 7). The regular cuboid boulder with the largest contact surface created a distinct splash in *z* direction (vertical).

Before the deceleration phase of all boulders, the response to the bore impact was similar. However, this changed after the impact of the second bore, when the flat cuboid boulder stopped immediately after 1.2 to 1.4 s, while the complex boulder reached its final position after about 1.9 s for the presented run.

The experiments showed that the longer the boulder was transported, the more the individual results diverged, in particular in the subaerial scenario. In the submerged and partially submerged scenarios, the results only spread over a small range. For the regular cuboid boulder, more experimental runs were necessary to reach a normalized distribution for transport distance (Figure S4, Table S2). Despite the irregular shape of the distribution groups (Figure S4), all experimental setups in Table 2 passed the D'Agostino & Pearson omnibus normality test, the Shapiro–Wilk normality test as well as the KS normality test, ensuring a statistically verified normal distribution of the results (Table S2). The 25% and 75% percentiles as well as the results for mean, minimum and maximum transport distances are also presented in Table 4.

Table 3. Time lag between bore impact and the initiation of boulder transport, averaged over all experimental runs

Boulder	Time lag between impact and mobilization (ms)
Regular cuboid	70
Complex	90
Flat cuboid	70

The idealized cuboid boulder was accelerated nearly to maximum velocity within the first third of the transport process (Figure 8). After the initial acceleration, it was transported with a fairly constant velocity. The deceleration phase was longer than the acceleration phase. The complex boulder had two phases of acceleration and deceleration. While the first acceleration phase was very short, the second acceleration and deceleration phase described a nearly Gaussian shape until the boulder reached its final position. The flat cuboid boulder reached its maximum velocity during the first acceleration phase, after which another lower and slightly broader peak occurred (Figure 8).

The experiments showed a strong influence of boulder shape on the total transport distance (Tables 5, 6, Figure S5). Depending on the extent of the initial submergence, the difference in total transport distance rose up to 900%, when the regular and flat cuboid boulders were compared in the partially submerged scenario. The influence of initial submergence was obvious for the flat cuboid boulder with an increased transport distance of 360% from partially submerged to subaerial. Focusing on the shape and the subaerial setup, the transport distance was strongly reduced between the regular cuboid and complex boulders (−35%) and also between the complex and flat cuboid boulder (−47.6%, Table 5). While the gap of the transport distances decreased between the regular cuboid and the complex boulders (−33.4%) for the partially-submerged setup, the gap increased between the complex and flat cuboid boulder (−85.2%). For the submerged case, the gap between the regular cuboid and the complex boulder increased again to 55.2%. The flat cuboid one showed no significant movement for the submerged case. The only observed transport mode was sliding.

Type 2 – non-uniform inclined shore model

For the subaerial experiments the boulders were placed 110 cm from the shore tip with their long axis (*a*-axis) perpendicular to the flow. When the bore reached the boulders, water was reflected in the *y* and *z* directions (0.06–0.16 s in Figure S6). After the initial impact between 0.0 and 0.06 s, the regular cuboid boulder started to move slowly with a velocity < 0.1 m/s and slightly rotated around the *a*-axis during transport (0.56–0.89 s). Approximately 0.89 s after the bore impact, the boulder rotated back into its original orientation. Between 0.09 s and 0.29 s, it moved with an average velocity of 0.57 m/s,

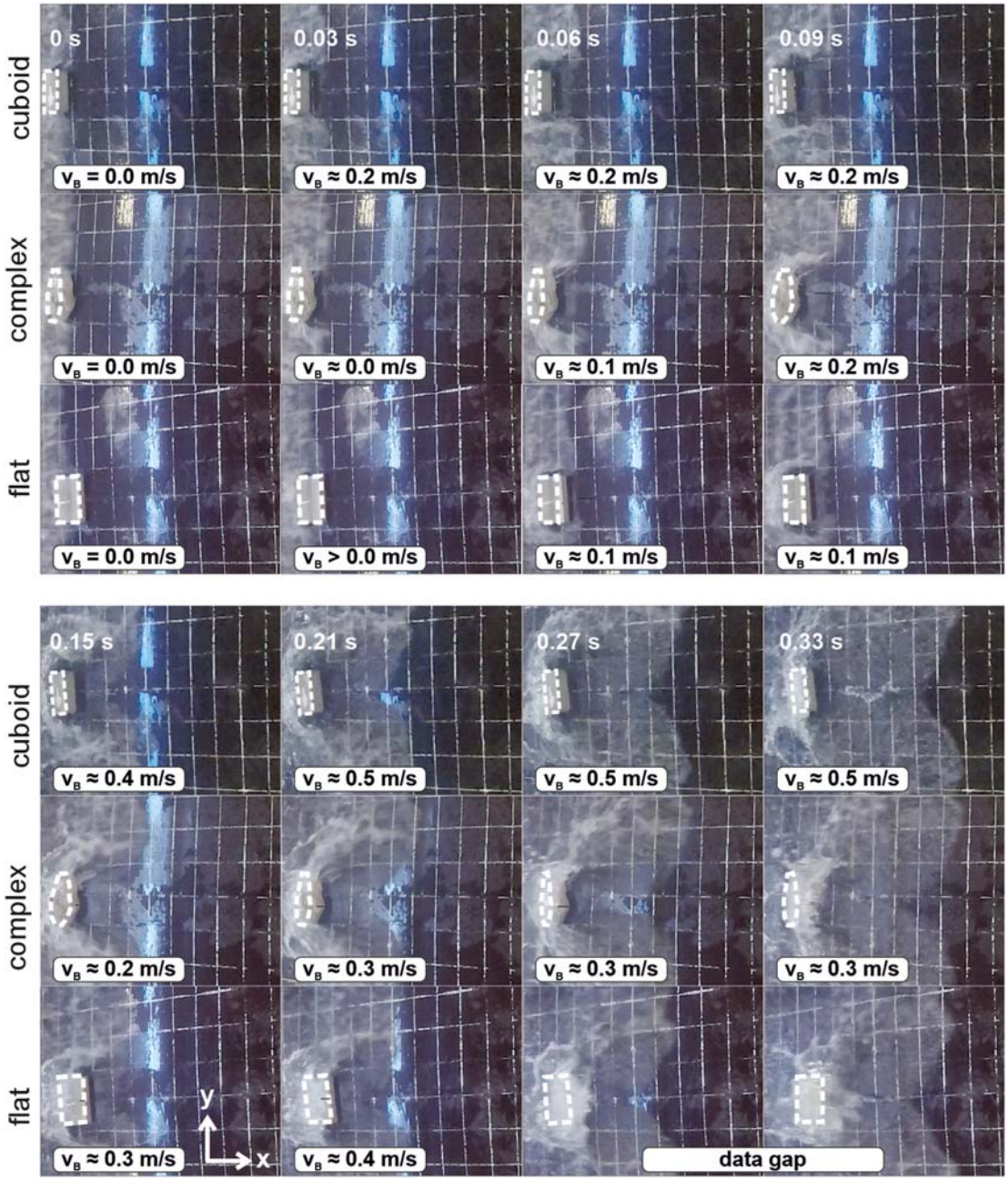

Figure 6. First 0.33 s of boulder movement in subaerial conditions (shore Type 1). The boulder velocity v_B is averaged between two presented timesteps and rounded to steps of 0.1 m/s since smaller differences are superimposed by uncertainties due to light refraction. [Colour figure can be viewed at wileyonlinelibrary.com]

compared to 0.52 m/s of the complex boulder. The discrepancy between the velocity of the regular cuboid (0.93 m/s) and complex (0.42 m/s) boulders increased to approximately 0.5 m/s before the complex boulder came to rest (Figures 9a, S6).

In the partially-submerged case, the boulders were placed 60 cm from the shore tip. The water reflection around the boulders and the initial splash were not as distinct as for the subaerial case (0.03–0.09 s in Figure S7). The complex boulder moved immediately after the bore impact, but only for a short distance. The regular cuboid boulder experienced a time gap between bore impact and the initiation of transport. After 0.22 s from the impact, the complex boulder was in motion and had passed the regular cuboid boulder by *c.* 10 cm (shown as red dotted circle in Figure 9a). After 0.90 s, the complex boulder was overtaken by the regular cuboid boulder, which again rotated slightly after bore impact (0.36 s). After 0.63 s, the regular cuboid boulder realigned the *a*-axis perpendicular to the flow leading to acceleration and a higher velocity. At the later stages, the distance between both boulders increased constantly, even though the regular cuboid boulder kept rotating its main axis horizontally for a few degrees to both sides. The complex boulder did not perform any significant rotation. While the regular cuboid boulder first turned anti-clockwise followed by a strong clockwise turn, the complex one shifted its main axis only slightly in both directions. The complex boulder came to rest after 3.30 s, while the regular cuboid boulder moved for 3.73 s, span for 0.27 s on the spot, and stopped eventually after 4.00 s (Figure 9b).

The results on shore Type 2 showed alignment and submergence as dominant parameters influencing transport distance. Furthermore, with longer transport distances, the discrepancy between the complex and regular cuboid boulders increased until the idealized regular cuboid boulder was shifted out of the experimental setup in nearly 50% of the subaerial cases for the 45° and 90° alignment (marked in Figures 10 and 11). This occurred only once for the

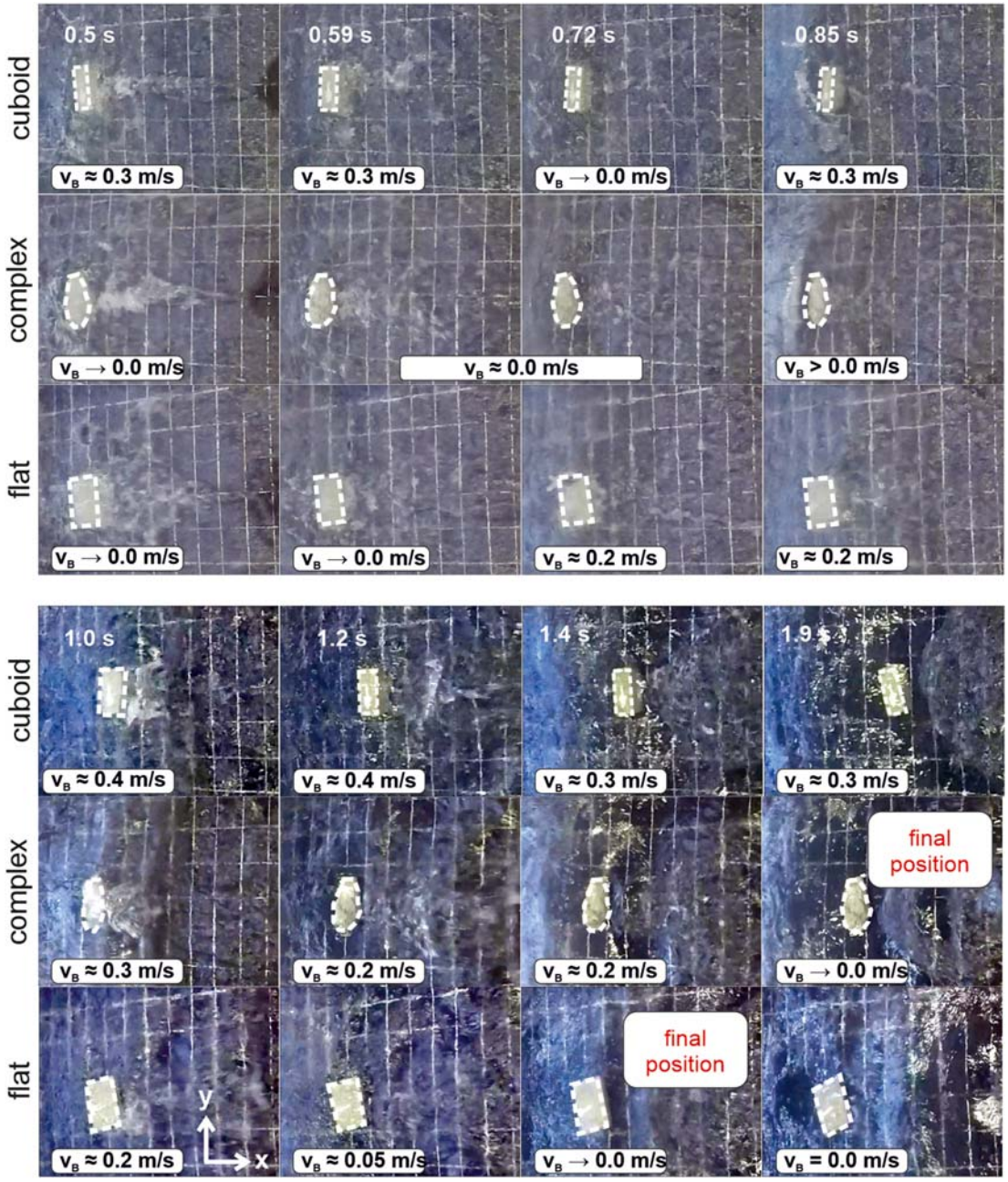

Figure 7. Boulder movement between 0.5 s and 1.9 s after wave impact in subaerial conditions (shore Type 1). The boulder velocity v_B is averaged between two presented timesteps and rounded to steps of 0.1 m/s, since smaller differences are superimposed by uncertainties due to light refraction. [Colour figure can be viewed at wileyonlinelibrary.com]

complex boulder (subaerial; 90° initial alignment). The increase can be explained by the lower energy transfer on the complex boulder during the bore impact. This effect is more obvious on longer transport distances since the available energy is directly dependent on the product of impact force and boulder impact area resulting in a non-linear

Table 4. Statistical results for the experiments on shore Type 1.

	Transport distance (cm)								
	Regular cuboid			Complex			Flat cuboid		
	sa	ps	s	sa	ps	s	sa	ps	s
Minimum	58.44	32.16	8.196	38.19	31.26	3.31	16.47	2.44	0.0
25% percentile	71.55	49.04	11.68	43.2	34.65	4.63	21.33	4.14	0.0
Median	75.61	54.23	12.03	47.25	36.12	5.39	24.78	5.34	0.0
75% percentile	83.27	63.18	14.51	50.27	41.61	6.19	26.95	7.92	0.0
Maximum	90.32	76.28	15.22	59.49	49.24	6.64	31.28	9.76	0.0
Mean	76.21	55.67	12.24	47.05	38.12	5.29	24.27	5.9	0.0

Note: sa, subaerial; ps, partially submerged; s, submerged.

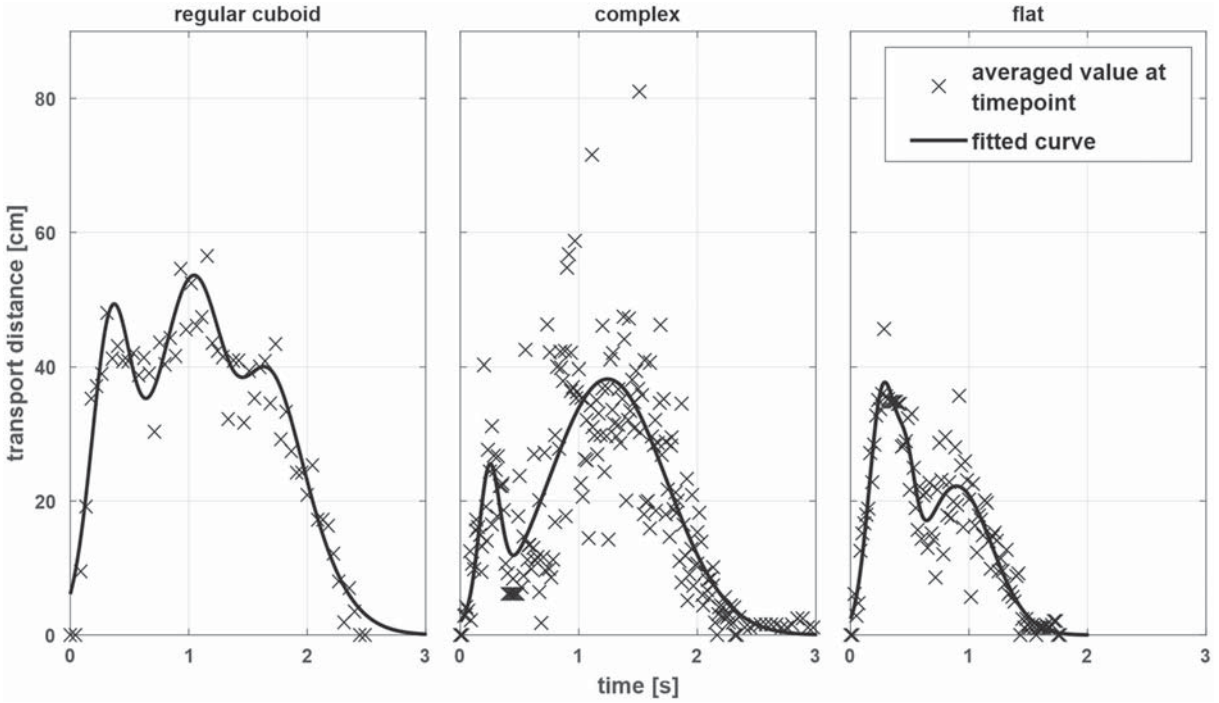

Figure 8. Transport over time for each tested boulder shape. The qualitative fitting curves are derived from the average displacements for multiple experimental runs (shore Type 1).

relationship between bore energy, boulder shape (or drag coefficient) and transport distance. The transport distance generally increased from the 0° to 90° alignment and from the submerged to subaerial setup. In all experiments except for the 0°, subaerial and partially-submerged cases, the 95% percentile of the regular cuboid boulder transport distance exceeds the distance of the complex one. Figure S8 shows the total transport distances on shore Type 2 grouped according to initial boulder alignment, submergence and boulder type (complex, regular cuboid).

Figures 10 and 11 show that pre-transport submergence was a more important control for transport distance than the impact angle of the wave. Between the submerged and the subaerial case, the transport distance increased by 2200% (excluding transportation beyond the step); between the submerged and partially-submerged scenarios, the distance increased by 1300%. Focusing on the impact angles 0° and 90°, the distance increased by 190%, and by 150% between 0° and 45° (excluding transportation out of the step). For impact angles of 0° and 45°, the boulders started to rotate around the *z*-axis (vertical axis) after the bore impact. After some back and forth rotation, the main axis aligned perpendicular to the flow.

In general, experimental runs on shore Type 2 showed a longer average transport distance for the regular cuboid boulder of approximately 90% (averaged over all submerged and partially-submerged setups) compared to the complex boulder.

Additional experiments showed a correlation between the initial water level in interaction with the pre-transport setting on the transport distance. For the submerged case, the transport distance increased when the boulder was placed in shallower water regions. The same was valid for the subaerial case: the closer the boulder was situated to the water's edge, the longer was the transport distance.

Type 3 – stepped shore platforms

The initial water level and wave parameters were altered over the experiments (Figures S9, S10). The variation of the initial water level became necessary since the submergence scenario could not be realized by simply changing the initial boulder position due to the stepped shore setup. Therefore, the pre-transport settings were realized using different initial water levels of 14 cm and 20 cm and two different steps of the model (Figure S11). Corresponding to the divergent initial water levels, the bore velocity also differed on this shore model.

In accordance with shore Types 1 and 2, the longest transport distances were measured for the subaerial setups (Figure S11). However, due to the experimental design, the maximum transport distance was limited to approximately 125 cm. The maximum transport distance for certain subaerial setups was therefore not measurable and set to an artificial maximum of 150 cm in Figure 11. From the distribution of transport distances of individual runs it becomes clear that the discrepancies with respect to the boulder shapes and the initial alignments are not as significant as in the other setups (Figure 11). The influence of the impact angle decreased substantially compared to shore Type 2 (Figures 10 and 11), while

Table 5. Transport distances grouped according to boulder shape and submergence (shore Type 1)

	Transport distances					
	Flat cuboid p-s	Complex p-s	Regular cuboid p-s	Flat cuboid sa	Complex sa	Regular cuboid sa
Average (cm)	5.9	38.1	55.7	24.3	47.0	76.2
Median (cm)	5.3	36.1	54.2	24.8	47.3	75.6

Note: sa, subaerial; ps, partially-submerged; s, submerged.

Table 6. Effect of boulder shape and submergence on the total transport distance in percentages (shore Type 1)

Ratio of transport distances					
Shape					
Flat cuboid p-s 100%	Complex p-s 677%	Regular cuboid p-s 1015%	Flat cuboid sa 100%	Complex sa 190%	Regular cuboid sa 305%
Flat cuboid 100%		Complex 433%		Regular cuboid 660%	
Submergence					
Flat cuboid p-s 100%	Flat cuboid sa 464%	Complex p-s 100%	Complex sa 131%	Regular cuboid p-s 100%	Regular cuboid sa 139%
ps 100%			sa 140%		

Note: sa, subaerial; ps, partially submerged; s, submerged.

submergence considerably affected the transport. The influence of the impact angle on the transport distance was almost negligible on shore Type 3 (shore Type 2: up to > 190% longer). Again, sliding was the only observed transport mode within the standardized experimental series and all boulders aligned their long axis perpendicular to the flow during the transport. During the experiments no boulder transport onto the next step was observed. However, vertical boulder transport would have been possibly caused by bores of significantly higher velocity and therefore height, which, however, were not part of the standardized experimental series analysed here. Particularly, in the partially-submerged cases, boulder movement was hampered due to wave reflection at the next vertical step (Figure 12).

Discussion

Parameter influence hierarchy

Identifying the parameter from the set of investigated parameters (boulder shape, shore type, submergence, alignment) with the strongest influence on boulder transport is not straightforward, mostly due to the synergy of the different parameters and the empirical nature of the study.

However, the experiments underline that the boulder shape (and its ground contact surface) needs to be considered as a parameter at least as important as the initial submergence for recalculating the necessary transport energy. The experiments show that the highest transport distances can be expected for configurations in which the wave impacts a subaerial boulder on its maximum possible contact surface. In contrast, a submerged boulder of comparable weight and volume but with only a small contact surface will be transported significantly shorter. The results indicate that a rounded boulder might be transported approximately a distance 30% shorter than an idealized cuboid boulder of comparable dimensions. However, in nature this effect of the boulder shape is possibly superimposed by other parameters, especially the initial submergence which showed an influence resulting in an increased transport distance of approximately 40% between partially-submerged and subaerial settings (shore Type 1). In particular the parameters submergence and alignment might amplify or attenuate each other leading to ranges of transport distances fitting to several combinations of initial submergence and alignment. Nevertheless, the influence of the boulder shape (beyond the Flatness Index), and also the aspect of roundness, is significant in all investigated setups and should therefore be considered when calculating boulder transport due to tsunamis or storm waves.

In the following paragraphs, first the general experimental sensitivity is evaluated followed by an analysis of initial alignment, shore type and boulder shape.

Experimental sensitivity

The results of the statistical analysis for shore Type 1 (uniformly inclined) showed clear trends, even though the number of experimental runs necessary to gain a normal distribution of transport distances differed significantly depending on boulder shape and initial boulder position (submerged, partially submerged, subaerial). In particular, the scatter of the transport distances, and therefore the number of necessary runs, increased with the average transport distance, i.e. from submerged to subaerial and from the regular flat boulder model to the complex shaped and the regular cuboid boulder (Figures 10, 11).

For several identical experimental setups of the same initial boulder position/alignment, initial water level, shore type and

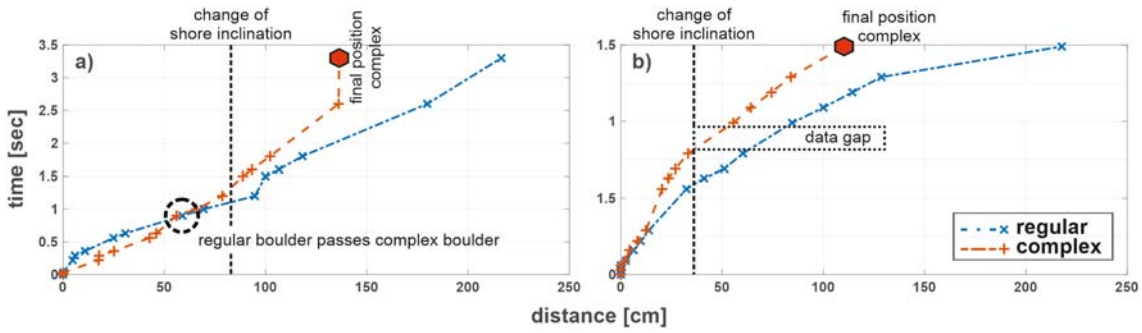

Figure 9. (a) Time-distance graph for the subaerial case at shore Type 2. (b) Time-distance graph for the partially-submerged case at shore Type 2. In both diagrams, the point of the changing shore inclination is marked by a dotted red line. [Colour figure can be viewed at wileyonlinelibrary.com]

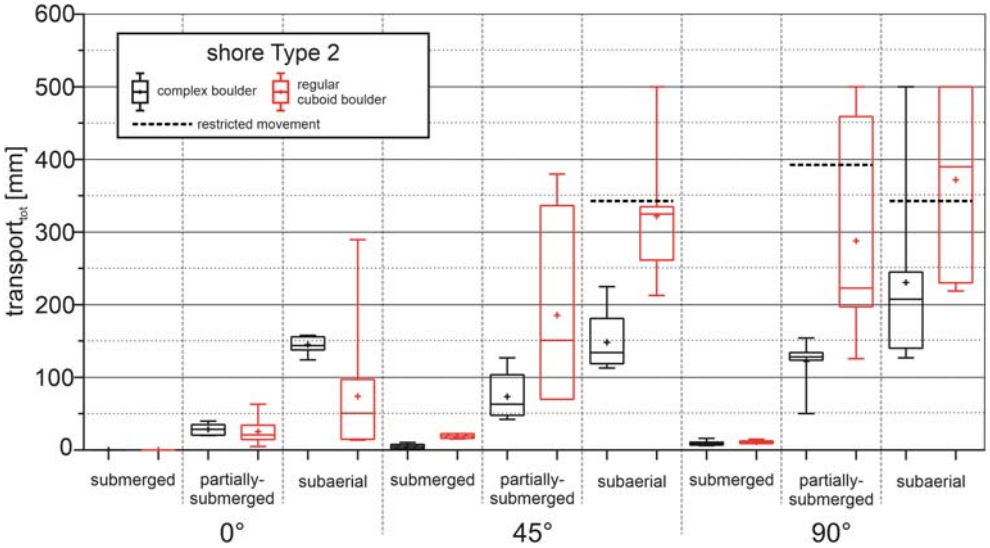

Figure 10. Comparison of the total transport distances grouped following the boulder shape (complex and regular cuboid), initial boulder alignment and submergence on shore Type 2. [Colour figure can be viewed at wileyonlinelibrary.com]

bore parameter, the transport distance varied by up to 650% (shore Type 2, complex boulder, submerged, 45°). In contrast, the transport distances within the 95% percentile of the regular cuboid boulder on shore Type 2 (subaerial, 0°) are significantly shorter than for the complex boulder, which is not in accordance to the overall trend. These deviations must be explained by very small, unavoidable differences between individual experimental runs, e.g. due to the highly turbulent flow, vibrations generated by the pumps and slight deviations (millimeter-scale) while placing the boulder manually in the model, especially regarding the alignment. However, the ability to create identical bores for two runs was already a significant improvement compared to experiments with dam-break type bore generation, especially if the dam break is initiated by manually opening the gate, and leads to sensitivity reduction. In Imamura et al. (2008), for example, high fluctuations of the transport distances have also been observed for repeated experiments (up to approximately 250%), although they occurred mainly for intermediate bore parameters and not for extrema. Despite the type of wave generation, the most obvious difference between the studies is the mean boulder size, which is significant smaller in Imamura et al. (2008). Thus, the larger gradient between the available impact energy (wave) and resisting forces (boulder) seems to superimpose fluctuations of the transport distances, leading to fewer fluctuations in the results.

Influence of shore type

It is remarkable that total transport distances of the three different boulder shapes differed much more in the inclined shore setups compared to the stepped one. Disregarding the subaerial cases due to the limitations on the stepped setup, the regular cuboid boulder on average reached 95% longer transport distances on shore Type 2 and 90% longer transport distances on shore Type 1, compared to the complex boulder. This difference disappears almost entirely in the stepped setup (shore Type 3). Furthermore, also the difference between the partially-submerged and subaerial setups as well as the difference between the initial alignments (0°, 45°, 90°) of the boulder is much smaller in the stepped shoreline scenario. The apparent influence of the shoreline morphology, however, has not been identified to be linear or easily

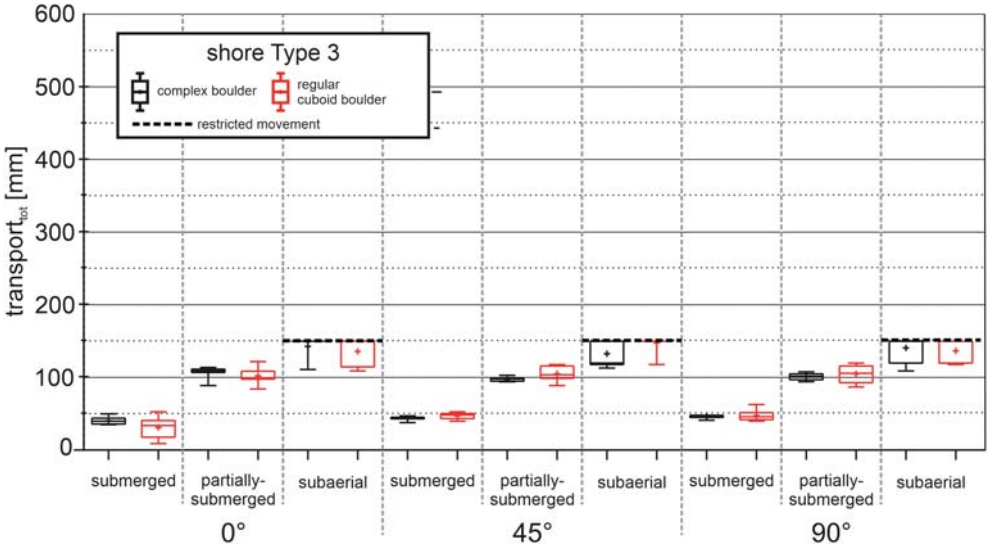

Figure 11. Comparison of the total transport distances grouped following the boulder shape (complex and regular cuboid), initial boulder alignment and submergence on shore Type 3. [Colour figure can be viewed at wileyonlinelibrary.com]

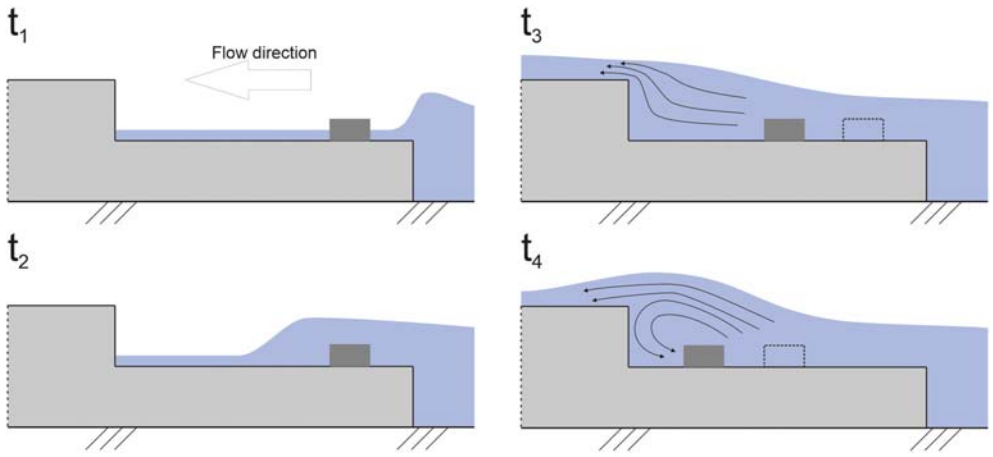

Figure 12. Movement-hampering influence of the stepped shore with partially-submerged setup (conceptual drawing). t_1: approaching bore, no boulder movement. t_2: bore reaches and overflows the boulder. No boulder movement. t_3: bore reaches next step and boulder is shifted along the flow direction. t_4: partial flow and wave reversing due to a hydraulic jump hamper the boulder movement. [Colour figure can be viewed at wileyonlinelibrary.com]

factorizable since the number of combinations of the other parameters (boulder shape, submergence, alignment, limited step length) has a major influence on the transport processes (e.g. Goto et al., 2010; Switzer and Burston, 2010; Nandasena and Tanaka, 2013). Further investigations with smaller step sizes and increased bottom roughness should be conducted in order to investigate the vertical transport of boulders.

Another observation from the partially-submerged cases on the stepped shore is that enough energy seems to be available for moving the boulder across the whole shore step but that it is slowed down due to flow reflection at the following shore step. Thus, the wave velocity is stopped and partly accelerated in the opposite direction. Since the boulder is not mobilized with the first wave impact and moves slower than the bore, its movement is reduced by the reflected wave resulting in a reduced transport distance (Figure 12). This hydraulic jump effect seems to superimpose the influence of boulder shape and impact angle and should be considered in field studies at comparable shoreline settings since reflections of the bore might occur even if the main part of the flow is still moving inland (e.g. Goto et al., 2010).

Initial boulder alignment to the flow

Liu et al. (2015) stated that a 45° pre-transport alignment leads to higher transport distances than 0° and 90°. In the present study, however, focusing on the complex boulder, transport distances of the 45° scenario were between those of 0° and 90°, which is in line with observations made by Nandasena and Tanaka (2013) for idealized shapes. In accordance with their findings, the transport distance in the 45° scenario exceeded the one in the 90° case for submerged boulders, but only by a nearly negligible amount in our findings. This indicates that the alignment only has a minor influence for submerged cases. For partially submerged and subaerial boulders we found the largest transport distances in the 90° scenario. This might be caused by the higher scale ratio (lower dimensions) applied in Liu et al. (2015). Nandasena and Tanaka (2013) found a reduced transport distance of 27% between an initial alignment of 0° and 90°. The present study confirms this observation as well as the fact that a boulder which was initially aligned with the long axis parallel to the flow tends to align with the long axis perpendicular to the flow after impact, as already indicated by Imamura et al. (2008). However, we found that the influence of the initial boulder alignment to be highly dependent on the shoreline configuration and observed a higher influence for an inclined shore and a much lower influence for a stepped shore.

We found a difference of the overall transport distance of approximately 5% on the horizontal stepped shore model. This difference rises up to nearly 670% on shore Type 2 for the partially submerged case. One reason for the deviation between the observations of Nandasena and Tanaka (2013) and our experiments could be the significantly larger impact area of the boulders applied in the present study. The largest applied boulder of Nandasena and Tanaka (2013) had an impact area of 32 cm^2 for the long boulder axis whereas the regular cuboid boulder of the present experiments has an impact area of 84 cm^2. Their boulder had an area of 16 cm^2 (48 cm^2 in our case) when the short axis was aligned with the flow. Hence, the ratio between the long and short axis is two in the case of Nandasena and Tanaka (2013) and 1.75 in the case presented here. The influence of the ratio between the long and the short impact area is possibly a transport-influencing parameter not investigated in detail so far and should be considered in future studies in addition to the Flatness Index (*sensu* Nandasena and Tanaka, 2013).

Boulder shape

Focusing on the boulder shape, the total transport distance was 47% longer for the regular cuboid boulder than for the complex shaped boulder (averaged over all partially-submerged setups). Experiments on the uniformly inclined shore Type 1 showed an additional transport distance of +177% for the complex shaped boulder compared with the flat cuboid boulder and a difference of +231% between the flat cuboid and the regular cuboid boulder. The results clearly showed the importance of boulder shape in tsunami-induced boulder transport and that this parameter needs to be considered beyond the Flatness Index, which is similar for the regular cuboid and the complex boulder deployed here. The shape determines the area available for wave impact in flow direction and defined by the *a* and *c* axis as well as the roundness of the boulder. It determines the drag force acting on the boulder, which, in combination with friction, is considered to be the dominant force controlling boulder transport by a tsunami (Goto et al., 2010;

Nandasena et al., 2011). Furthermore, the drag coefficient and, thus, the energy transferred from the bore probably increases first from the complex to the regular cuboid, and further to the flat cuboid boulder. From the experiments it seems that the effect of the (presumably) higher drag coefficient of the flat cuboid boulder is superimposed by the higher ground-contact area compared to the other shapes. Based on our experiments, this is the most reasonable explanation for the shorter transport distance of the flat cuboid boulder, but further investigations of the dependencies between the coefficients of drag and friction on transport distance are needed.

However, since we conducted experiments with three boulder models of relatively large variations in shape, the datasets are not yet sufficient to develop meaningful conclusions and (analytical or numerical) models considering the shape overcoming idealized (cuboid) shapes. Considering the sensitive boulder behaviour in the flow, it might be an option to conduct experimental series focusing on several boulder models with smoothly changing shapes in the future, e.g. from egg-like to cuboid by holding all other parameter constant and repeating the experiments for each boulder shape until a statistically robust result is reached.

General observations

The comparison of the flow fields around the complex and regular cuboid boulders shows how the flow responds to boulder shape (Figures 13, S6). The highly turbulent flow field around the regular cuboid boulder occurring immediately after the impact shows a clear disruption of the flow in front of and behind the boulder. This provides evidence that a high amount of energy is transferred from the bore to the boulder. For the complex boulder, turbulences are less distinct and more water is diverted around the boulder, which indicates lower energy transfer.

Nandasena and Tanaka (2013) analysed the flow field around the boulder within the first 0.3 s after bore impact. Interestingly, the authors describe the flow after the impact as opening towards the flow direction, while in the present study the flow field was found to already close after 0.1 s in the case of the regular cuboid boulder model (Figure 13). After 0.2 s, Nandasena and Tanaka (2013) found the stream closing in flow direction where we identified the beginning of the closing process a length from the boulder away both for the regular cuboid and the complex shaped boulder. A reason for the different observations might be the higher maximum Froude number in our

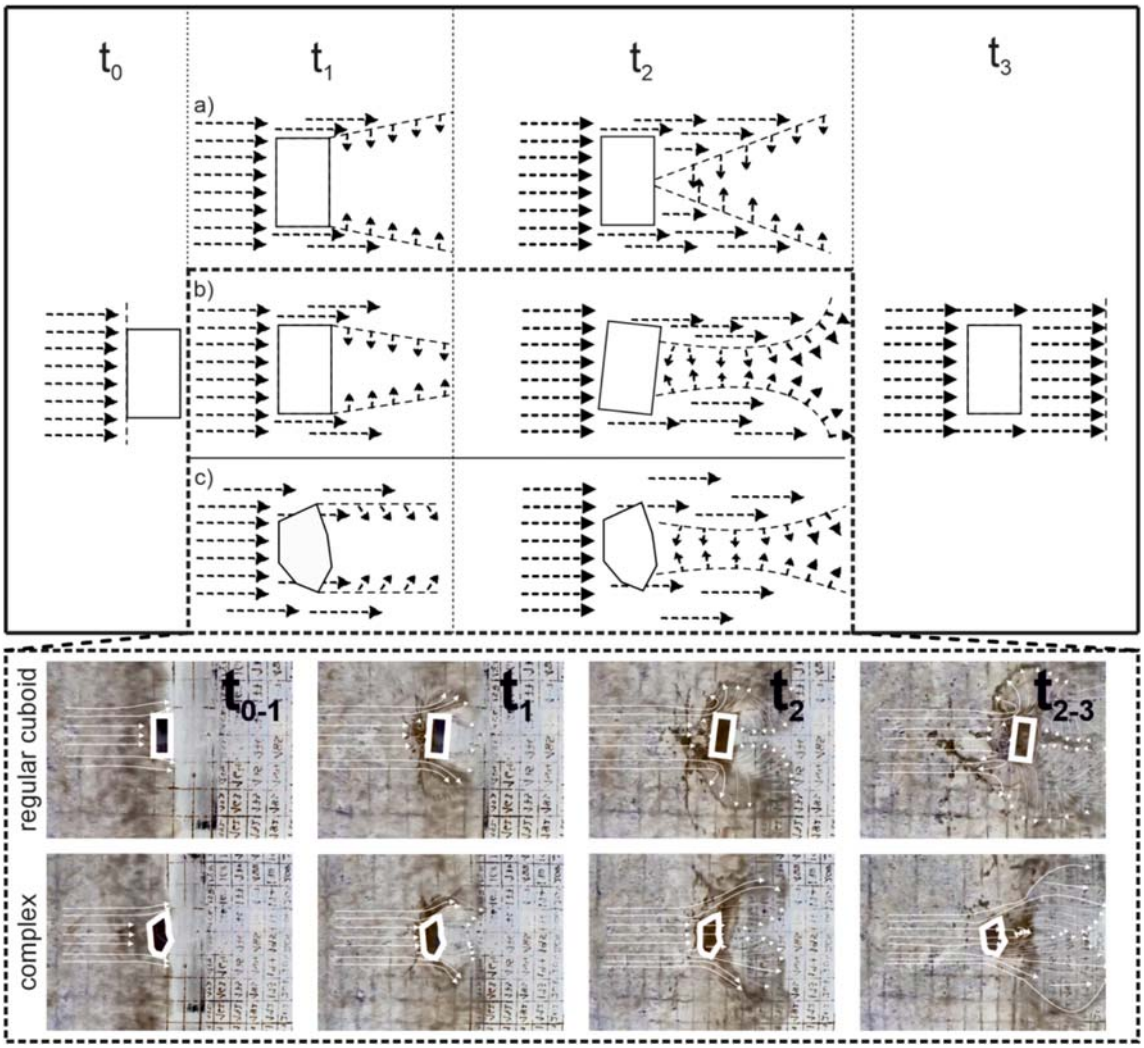

Figure 13. Comparison between the simplified horizontal flow fields of (a) Nandasena and Tanaka (2013), (b) the regular cuboid boulder, (c) the complex boulder. For the regular cuboid and complex boulder time step two and three are shown as photographs, depicting the flow field around the boulder in higher detail. We found a 'trumpet' like flow field behind the boulder where Nandasena and Tanaka (2013) published a more straight-lined field. Time interval between states is 0.1 s (series a and design from Nandasena and Tanaka, 2013, modified). [Colour figure can be viewed at wileyonlinelibrary.com]

experiments resulting in higher flow velocities on the shore creating a larger and longer stable area almost free of flow perpendicular to the main flow direction. From the video snapshots in Figure 13 it can be seen that the flow field closes significantly faster in the case of the complex boulder compared to the regular cuboid. This observation underlines the lower transfer of energy resulting in shorter transport distances originating from the streamline shape (lower drag coefficient) and boulder parts without ground contact.

We found several agreements with the experimental results in Liu et al. (2015). Liu et al. (2015) state that the boulder reached a velocity of approximately 50% of that of the bore in front of the shore which is in accordance with our results. Furthermore, they found three basic phases in the boulder transport process: acceleration, steady and deceleration phase. We found an additional second acceleration phase for the inclined shore setups, but are able to confirm the three-phase transport process on the horizontally stepped shore setup.

As in Liu et al. (2015), we also found sliding as the general transportation mode for tsunami induced boulder transport. In the present study, overturning of the boulder occurred only in three of over 600 experimental runs, and even in those cases was the boulder overturned only once and then transported further by sliding. However, the transport mode depends significantly on roughness- and bathymetry-related parameters and shape (flatness, sphericity) and it has a strong influence on the transport distance (Imamura et al., 2008; Nandasena and Tanaka, 2013). Since rolling and saltating are quite common field observations, in particular in very rough, karstified limestone settings (Etienne et al., 2011; Engel and May, 2012; May et al., 2015), further research is required as those transport modes are assumed to increase the transport distance due to reduced friction and centrifugal forces (e.g. Imamura et al., 2008).

Nandasena and Tanaka (2013) also conducted statistical analyses of the dependencies between several boulder parameters (boulder main axis, Flatness Index, block weight) and the transport distance. They found the highest determination coefficient for the influence of the weight of the boulder (R^2 = 0.7115), followed by the length of its main axis (approximately R^2 = 0.35). Both parameters were not considered in our study. However, Nandasena and Tanaka (2013) found the weakest correlation for the FI with R^2 = 0.05. Even though we only applied three different boulder shapes (compared to 15 in Nandasena and Tanaka, 2013), the statistical analyses of the experiments on the uniformly inclined shore (shore Type 1) indicate that the FI needs to be modified in order to consider shapes other than idealized, cuboid shapes.

Future directions and numerical investigations

Data and observations from this study will be used for validating a new numerical approach based on the two-phase mass flow model of Pudasaini (2012). Here, a numerical two-phase mass flow model is enhanced for tsunami-induced boulder transport by implementing the boulder as a floating immersed boundary (immersed boundary method, e.g. Peskin, 2002). Once the numerical model is successfully validated for boulder transport induced by single-phase waves, further physical experiments and numerical investigations will be conducted enhancing the bore as a solid-fluid mixture. The influence of the sedimentary load within the wave is already under discussion but has not been investigated in detail so far (e.g. Kain et al., 2012). The model of Pudasaini (2012) is already widely accepted for modelling two-phase mass flows as well as mass flow-induced tsunamis (e.g. Mergili et al., 2017; Mergili et al., 2018; Drenkhan et al., 2019; Pudasaini and Mergili, 2019), and therefore provides an excellent opportunity for investigating the influence of a second phase on tsunami-induced boulder transport.

The validation of other numerical models would benefit from further improvements regarding the experimental design. Obtaining information of the flow in greater detail could be achieved by employing boulders of contrasting colour (cf. Cox et al., 2019) and to use e.g. particle-image-velocimetry (PIV) techniques for tracking the streamlines. The highly turbulent flow around the boulder incorporating air in the flow might provide enough information for such approaches. Additional information could be gained from front or rear-view video recordings which would enable analysis of the flow behaviour on every side of the boulder. In our experiments, several factors need to be considered regarding the lack of vertical transport of the boulders in the stepped shoreline model (Type 3): Firstly, the wave length may have been too short, resulting in an insufficiently long acting lift force. In contrast, the wave might have been too steep and not able to generate sufficient lift underneath the boulder before following water hampered a potential lift from the platform. Additionally, the smooth ground surface of the model supported a sliding motion of the boulders, which also impeded a possible lift since the energy of the wave is hindered to generate a sufficient lift force underneath the boulder (e.g. due to tilting).

The experiments showed the strong influence of the boulder shape on the transport process. Therefore, we recommend to apply a dimensionless factor summarizing not only the ratio of the three dimensions of an idealized boulder model but furthermore accounting for the 'energetic' shape of the boulder which is related to the impact area. This could be done by introducing a coefficient accounting for both the flatness and the drag coefficient of the boulder, as well as its roundness, which can be systematically quantified in the field (Cox et al., 2018). The empirical derivation of such a coefficient would need a number of experiments based on smooth shape variations from angular-cubic to smooth-spherical by holding the same wave and shore parameter, for example. Therefore, investigating further boulder shapes with only slightly altered forms could help to obtain a better understanding of the processes during bore impact and to derive meaningful numerical and analytical models.

Conclusions

Boulder transport by high-energy waves is a sensitive process and investigations based on physical experiments require a well-controlled environment. The presented experiments clearly show the influence of boulder shape and initial submergence of the boulder on the transport distance. With decreasing available impact area on the boulder, which is also related to roundness, the transport distance decreases as well. However, the influence of the shape almost vanishes on the investigated stepped shore, indicating that the effect of the boulder shape decreases with decreasing shore inclination. Future in-field, numerical and experimental investigations should therefore also systematically target different shore types and consider their influence on boulder transport.

Investigations of the flow-field around the boulder indicate that the flow disruption is significantly larger for the regular and idealized cuboid boulder than for the complex one. This observation underlines that less energy is transferred from the bore to the streamlined, complex boulder resulting in shorter transport distances compared to the cuboid boulder. The

divergence between the complex and idealized boulders increases further for longer transport distances due to the non-linear correlation between boulder drag coefficient, impact force, friction and transport distance.

As a next step, an idealized (cuboid) shape could be incrementally adjusted to a natural shape (e.g. like the BOL 2 from Bonaire considered here) with several stages in between to elaborate coefficients exceeding the typical range of applied drag coefficients and flatness numbers.

For validation and calibration issues on numerical boulder transport models, the gained data provide a useful database even if the deviation of results needs to be handled carefully. For future investigations regarding the interaction of particle-laden flows and boulders, the extent of experimental setups will have to be reduced (comparable to presented shore Type 1) in order to gain robust baseline data overcoming ambiguities in statistical significance.

Acknowledgements—This contribution received funding by the German Research Foundation (Deutsche Forschungsgemeinschaft, DFG) for the project 'Modelling tsunami-induced coarse-clast transport – combination of physical experiments, advanced numerical modelling and field observations' (SCHU 1054/7-1, EN 977/3-1).

Shiva P. Pudasaini gratefully acknowledges the financial support provided by the German Research Foundation (DFG) through the research project, PU 386/5-1: 'A novel and unified solution to multi-phase mass flows'.

Data availability statement

The data sets used and/or analysed during the current study are available from the corresponding author on reasonable request.

Statement of interest

The authors declare no conflict of interest. The funders had no role in the design of the study; in the collection, analyses, or interpretation of data; in the writing of the manuscript, or in the decision to publish the results.

References

Blair TC, McPherson JG. 1999. Grain-size and textural classification of coarse sedimentary particles. *Journal of Sedimentary Research* **69**(1): 6–19. https://doi.org/10.1306/D426894B-2B26-11D7-8648000102C1865D.

Boesl F, Engel M, Eco RC, Galang JA, Gonzalo LA, Llanes F, Quix E, Brückner H. 2019. Digital mapping of coastal boulders – high-resolution data acquisition to infer past and recent transport dynamics. *Sedimentology*, **67**(3): 1393-1410. https://doi.org/10.1111/sed.12578.

Bourrouilh-Le Jan FG, Talandier J. 1985. Sédimentation et fracturation de haute énergie en milieu récifal: tsunamis, ouragans et cyclones et leurs effets sur la sédimentologie de la géomorphologie d'un atoll: motu et hoa, à Rangiroa, Tuamotu, SE Pacifique. *Marine Geology* **67**: 263–333. https://doi.org/10.1016/0025-3227(85)90095-7.

Bressan L, Guerrero M, Antonini A, Petruzzelli V, Archetti R, Lamberti A, Tinti S. 2018. A laboratory experiment on the incipient motion of boulders by high-energy coastal flows. *Earth Surface Processes Landforms* **43**(14): 2935–2947. https://doi.org/10.1002/esp.4461.

Cox R, Lopes WA, Jahn KL. 2018. Quantitative roundness analysis of coastal boulder deposits. *Marine Geology* **396**: 114–141. https://doi.org/10.1016/j.margeo.2017.03.003.

Cox R, O'Boyle L, Cytrynbaum J. 2019. Imbricated coastal boulder deposits are formed by storm waves, and can preserve a long-term storminess record. *Scientific Reports*, **9**: 10784. https://doi.org/10.1038/s41598-019-47254-w

Drenkhan F, Huggel C, Guardamino L, Haeberli W. 2019. Managing risks and future options from new lakes in the deglaciating Andes of Peru: The example of the Vilcanota-Urubamba basin. *Science of the Total Environment* **665**: 465–483. https://doi.org/10.1016/j.scitotenv.2019.02.070.

Engel M, May SM. 2012. Bonaire's boulder fields revisited: Evidence for Holocene tsunami impact on the Leeward Antilles. *Quaternary Science Reviews* **54**: 126–141. https://doi.org/10.1016/j.quascirev.2011.12.011.

Engel M, Oetjen J, May M, Brückner H. 2016. Tsunami deposits of the Caribbean – towards an improved coastal hazard assessment. *Earth-Science Reviews* **163**: 260–296. https://doi.org/10.1016/j.earscirev.2016.10.010.

Etienne S, Buckley M, Paris R, Nandasena AK, Clark K, Strotz L. 2011. The use of boulders for characterising past tsunamis: Lessons from the 2004 Indian Ocean and 2009 South Pacific tsunamis. *Earth-Science Reviews* **107**(1-2): 76–90. https://doi.org/10.1016/j.earscirev.2010.12.006.

Gienko GA, Terry JP. 2014. Three-dimensional modeling of coastal boulders using multi-view image measurements. *Earth Surface Processes and Landforms* **38**: 853–864. https://doi.org/10.1002/esp.3485.

Goto K, Okada K, Imamura F. 2010. Numerical analysis of boulder transport by the 2004 Indian Ocean tsunami at Pakarang Cape, Thailand. *Marine Geology* **268**: 97–105. https://doi.org/10.1016/j.margeo.2009.10.023.

Imamura F, Goto K, Ohkubo S. 2008. A numerical model for the transport of a boulder by tsunami. *Journal of Geophysical Research* **113**: C01008. https://doi.org/10.1029/2007JC004170.

Kain CL, Gomez C, Moghaddam AE. 2012. Comment on 'Reassessment of hydrodynamic equations: Minimum flow velocity to initiate boulder transport by high energy events (storms, tsunamis)', by N.A. K. Nandasena, R. Paris and N. Tanaka [Marine Geology 281, 70–84]. *Marine Geology* **319**: 75–76.

Liu H, Sakashita T, Sato S. 2015. An experimental study on the tsunami boulder movement. *Coastal Engineering Proceedings* **34**: currents.16. https://doi.org/10.9753/icce.v34.currents.16.

May SM, Engel M, Brill D, Cuadra C, Lagmay AMF, Santiago J, Suarez K, Reyes M, Brückner H. 2015. Block and boulder transport in eastern Samar (Philippines) during Supertyphoon Haiyan. *Earth Surface Dynamics* **3**: 543–558. https://doi.org/10.5194/esurf-3-543-2015.

Mergili M, Emmer A, Juřicová A, Cochachin A, Fischer J-T, Huggel C, Pudasaini SP. 2018. How well can we simulate complex hydro-geomorphic process chains? The 2012 multi-lake outburst flood in the Santa Cruz Valley (Cordillera Blanca, Perú). *Earth Surface Processes and Landforms* **43**: 1373–1389. https://doi.org/10.1002/esp.4318.

Mergili M, Fischer JT, Krenn J, Pudasaini SP. 2017. r.avaflow v1, an advanced open-source computational framework for the propagation and interaction of two-phase mass flow. *Geoscientific Model Development* **10**: 553–569. https://doi.org/10.5194/gmd-10-553-2017.

Nakata T, Kawana T. 1995. Historical and prehistorical large tsunamis in the southern Ryukyus, Japan. In *Tsunami: Progress in Prediction, Disaster Prevention and Warning*, Tsuchiya Y, Shuto N (eds). Springer: Dordrecht; 211–221 https://doi.org/10.1007/978-94-015-8565-1_15.

Nandasena NAK. 2020. Perspective of incipient motion formulas: boulder transport by high-energy waves. In *Geological records of tsunamis and other extreme waves*, Engel M, Pilarczyk J, May SM, Brill D, Garrett E (eds). Elsevier: Amsterdam.

Nandasena NAK, Paris R, Tanaka N. 2011. Reassessment of hydrodynamic equations: Minimum flow velocity to initiate boulder transport by high energy events (storms, tsunamis). *Marine Geology* **281**: 70–84. https://doi.org/10.1016/j.margeo.2011.02.005.

Nandasena NAK, Tanaka N. 2013. Boulder transport by high energy: Numerical model-fitting experimental observations. *Ocean Engineering* **57**: 163–179. https://doi.org/10.1016/j.oceaneng.2012.09.012.

Neale P.. 1885. The Krakatoa Eruption. *The Leisure Hour*, **34**, 348–351; 379–388; 544–557; 635–638. (The contribution is cut into several sections distributed in this volume).

Noormets R, Crook KAW, Felton EA. 2004. Sedimentology of rocky shorelines: 3. Hydrodynamics of megaclast emplacement and transport on a shore platform, Oahu, Hawaii. *Sedimentary Geology* **172** (1-2): 41–65. https://doi.org/10.1016/j.sedgeo.2004.07.006.

Nott J. 1997. Extremely high-energy wave deposits inside the Great Barrier Reef, Australia. Determining the cause—tsunami or tropical cyclone. *Marine Geology* **141**(1-4): 193–207. https://doi.org/10.1016/S0025-3227(97)00063-7.

Nott J. 2003. Waves, coastal boulder deposits and the importance of the pre-transport setting. *Earth and Planetary Science Letters* **210**(1-2): 269–276. https://doi.org/10.1016/S0012-821X(03)00104-3.

Oetjen J, Engel M, Brückner H, Pudasaini SP, Schüttrumpf H. 2017. Enhanced field observation-based physical and numerical modelling of tsunami-induced boulder transport. Phase I: Physical experiments. *Coastal Engineering Proceedings* **35**: management.4. https://doi.org/10.9753/icce.v35.management.4.

Oetjen J, Schüttrumpf H, Engel M. 2020. Experimental models of coarse-clast transport by tsunamis. In *Geological records of tsunamis and other extreme waves*, Engel M, Pilarczyk J, May SM, Brill D, Garrett EG (eds). Elsevier: Amsterdam.

Paris R, Fournier J, Poizot E, Etienne S, Morin J, Lavigne F, Wassmer P. 2010. Boulder and fine sediment transport and deposition by the 2004 tsunami in Lhok Nga (western Banda Aceh, Sumatra, Indonesia): A coupled offshore–onshore model. *Marine Geology* **268**: 43–54. https://doi.org/10.1016/j.margeo.2009.10.011.

Pedersen G, Gjevik B. 1983. Run-up of solitary waves. *Journal of Fluid Mechanics* **135**: 283–299. https://doi.org/10.1017/S0022112083003080.

Peskin CS. 2002. The immersed boundary method. *Acta Numerica* **11**: 479–517. https://doi.org/10.1017/S0962492902000077.

Pignatelli C, Sansò P, Mastronuzzi G. 2009. Evaluation of tsunami flooding using geomorphologic evidence. *Marine Geology* **260**(1-4): 6–18. https://doi.org/10.1016/j.margeo.2009.01.002.

Pudasaini SP. 2012. A general two-phase debris flow model. *Journal of Geophysical Research* **117**: F03010. https://doi.org/10.1029/2011JF002186.

Pudasaini SP, Mergili M. 2019. A multi-phase mass flow model. *Journal of Geophysical Research: Earth Surface* **124**: 2920-2942. https://doi.org/10.1029/2019JF005204.

Scheffers A, Kelletat D. 2003. Sedimentologic and geomorphologic tsunami imprints worldwide – a review. *Earth-Science Reviews* **63**: 83–92. https://doi.org/10.1016/S0012-8252(03)00018-7.

Sugawara D, Goto K, Jaffe BE. 2014. Numerical models of tsunami sediment transport — current understanding and future directions. *Marine Geology* **352**: 295–320. https://doi.org/10.1016/j.margeo.2014.02.007.

Switzer AD, Burston JM. 2010. Competing mechanisms for boulder deposition on the southeast Australian coast. *Geomorphology* **114**: 41–54. https://doi.org/10.1016/j.geomorph.2009.02.009.

Watanabe M, Goto K, Imamura F, Kennedy A, Sugawara D, Nakamura N, Tonosaki T. 2019. Modeling boulder transport by coastal waves on cliff topography: Case study at Hachijo Island, Japan. *Earth Surface Processes and Landforms* **44**: 2939–2956. https://doi.org/10.1002/esp.4684.

Watt, SG, Jaffe, BE, Morton, RA, Richmond, BM, Gelfenbaum, G. (2010). Description of Extreme-wave Deposits on the Northern Coast of Bonaire, Netherlands Antilles, Netherlands Antilles. USGS Open-file Report, 2010-1180. US Geological Survey, Reston, VA. https://doi.org/10.3133/ofr20101180

Zainali A, Weiss R. 2015. Boulder dislodgement and transport by solitary waves: Insights from three-dimensional numerical simulations. *Geophysical Research Letters* **42**: 4490–4497. https://doi.org/10.1002/2015GL063712.

Supporting Information

Additional supporting information may be found online in the Supporting Information section at the end of the article.

Figure S1. Repeated wave generation. (a) Comparison of wave velocity. (b) Comparison of wave-height.

Figure S2. Wave profile on shore Type 1. Measured 1.5 m in front of the shore tip.

Figure S3. Distances between shore tip and boulder models depending on initial submergence and boulder type.

Figure S4. Distribution graphs for the transport distances on shore Type 1.

Figure S5. Box plot for the maximum transport distances on shore Type 1. Grouped following submergence and boulder shape. The initial orientation was kept as 90° (long axis perpendicular to the flow) over all experiments on shore Type 1.

Figure S6. Optical comparison between the transport process of the complex and regular cuboid boulder on shore Type 2, partially submerged and 90° initial alignment (representative experimental run).

Figure S7. Optical comparison between the transport process of the complex and regular cuboid boulder on shore Type 2, subaerial and 90° initial alignment (representative experimental run).

Figure S8. Total transport distances on shore Type 2 grouped for boulder shape based on 131 experiments (black: complex; red: regular cuboid boulder). Only unidirectional flow and no backwash is considered.

Figure S9. Wave profiles for all generated waves on shore Type 3.

Figure S10. Initial boulder positions and water level for the experiments on the stepped shore.

Figure S11. Total transport distances on shore Type 3 grouped for boulders (black: complex; red: regular cuboid boulder). The red line marks the transport limit (extended movements are set to step size in the figure).

Table S1. Overview for the conducted experiments on shore Type 1.

Table S2. Statistical results for the experiments on shore Type 1.

